Experiments using a 525 nm time-of-flight camera for object imaging and ranging in clear and turbid water

Luke Rumbaugh*[a], John Will[a], Joshua Thomson[a], Austin Jantzi[b], William Jemison[b], David Illig[c],

[a]Dept. of Electrical and Computer Engineering, Grove City College, 100 Campus Dr., Grove City, PA, USA 16127; [b]Dept. of Electrical and Computer Engineering, Clarkson University, 8 Clarkson Ave, Potsdam, NY, USA 13699-5720; [c]Warfighter Basic and Applied Research Division, Naval Air Warfare Center, 22347 Cedar Point Rd., Patuxent River, MD, USA, 20670

ABSTRACT

This paper presents experiments using a time of flight (ToF) camera modified to use 525 nm green laser illumination to capture amplitude and depth images of an underwater scene. Experiments in object imaging and ranging were conducted in both clear and turbid water. 3D imaging using flood illumination was successfully performed in clear water and in some turbid water conditions. Ranging using collimated laser beams was performed in turbid water. Several major error sources were observed, including low illumination levels, fixed pattern noise, and backscatter contribution to the phase measurement. To attempt to address these concerns, multiple lasers were used to improve illumination levels and spatial frequency domain filtering was performed to mitigate fixed pattern noise. Additionally, experiments with using multiple modulation frequencies suggested that there may be potential for discriminating backscatter from object reflection.

Keywords: Lidar, underwater, underwater imaging, time-of-flight cameras, ToF, lasers, mapping

1. INTRODUCTION

Time-of-flight (ToF) cameras have become widely used tools for 3D mapping and modeling [1, 2]. ToF cameras record both reflectivity and distance for every pixel of every frame, generating grayscale amplitude images and depth images [3]. They have several attractive attributes including: video-speed frame rates; centimeter-order depth resolution; consistent depth accuracy that does not change with operating range; minimal post-processing requirements; small footprint; and excellent ambient light rejection [4]. As of 2022, their drawbacks include low pixel count (a focus of recent hardware development [5]) and multi-path interference (a focus of recent software/firmware development [6]).

This paper describes recent experiments conducted as part of an underwater ToF camera investigation. The goal of this project is to evaluate the suitability of ToF cameras for use in ranging and imaging underwater, both in clear and in turbid water. This paper presents hardware and software upgrades from a previous version of this custom camera [7], shows experimental work in both clear and turbid water, and discusses where the ToF camera seemed to perform well and where we found drawbacks. The ToF camera used for experiments has three 1 W 525 nm laser diodes and is based on a modified Espros EPC660 evaluation kit [8].

2. TOF CAMERA DESIGN

The customized ToF camera prototype used is shown in Figure 1. This camera is based on the Espros EPC660 evaluation kit. The kit uses the 320x240 pixel EPC660 sensor and was chosen because it has no built-in infrared filter and so can be used with visible light. The sensor outputs four 12-bit differential correlation samples (DCS) images per frame. These DCS images are combined to form an amplitude image and a depth image. The EPC660 chip generates a digital timing signal used to drive the illuminating lasers, and computes the DCS images by demodulating the received optical signal at each pixel using this timing signal. In our custom setup, a signal breakout board (the “SigBoard”) breaks out the timing signal, buffers it, and routes it to a custom laser driver board (the “LightBoard”). The LightBoard uses a MOSFET switching circuit to drive Nichia NUGM03 1 W 525 nm laser diodes. These lasers operate at 1.5 A peak current and are switched as dictated by the digital timing signal. Each laser is mounted in a heat sink and has a removable diffuser. Two

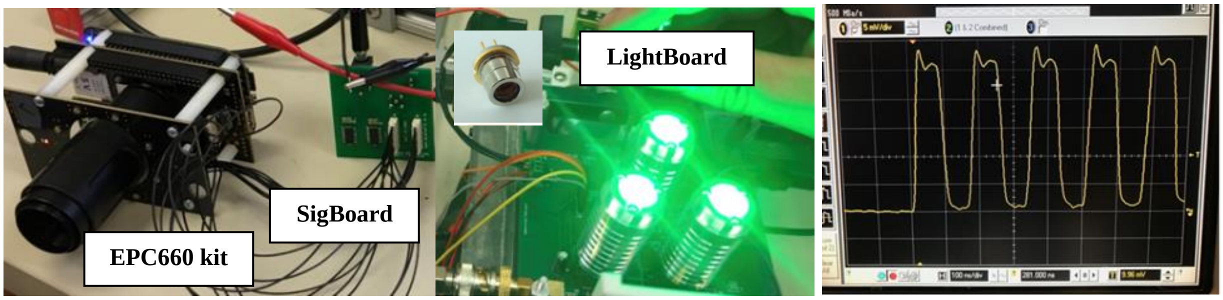

Figure 1. Camera hardware. *Left*: The Espros EPC660 evaluation kit is the core of the camera. A small breakout board "SigBoard" passes the digital timing signal to the green laser board. *Center*: The green laser driver "LightBoard" uses three lasers to illuminate the scene. *Center inset*: The LightBoard uses 1 W 525 nm TO-9 diode lasers. *Right:* Transmitted camera illumination waveforms as read by a photodetector using a modulation frequency of 12 MHz.

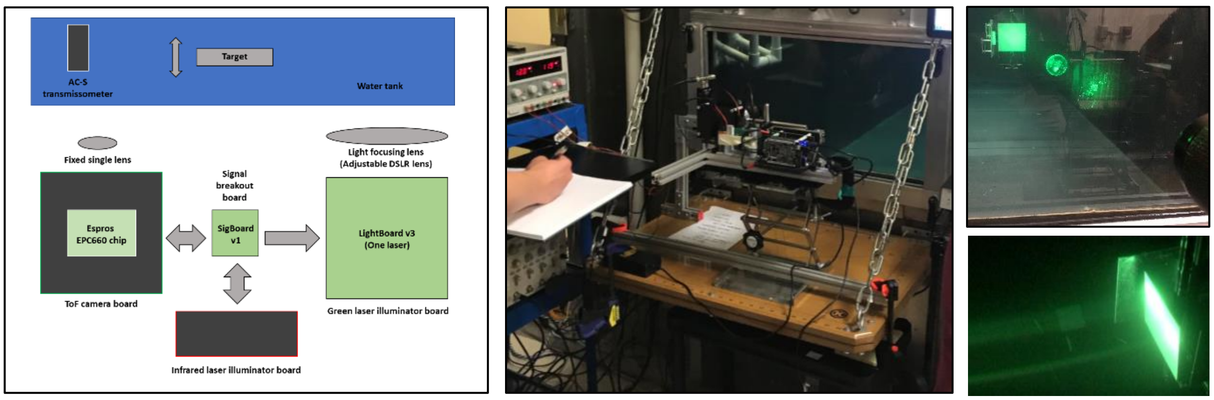

Figure 2. Experimental setup for clear water baseline experiments. *Left:* Block diagram for experiments. *Center:* Photograph of camera looking into input window of water tank. *Right:* Images of the submerged gray plate illuminated by the green laser light.

versions of the LightBoard were used: a one-laser version was used for clear water, but after starting experimentation in turbid water we built another version with three lasers. The camera receiver has a fixed 35 mm plano-convex lens and a KG3 infrared light blocking filter in the optical tube in front of the sensor.

Each camera frame uses a burst of high-frequency square wave modulation to perform continuous-wave (CW) ToF measurements. The square wave frequency is set to one of a discrete set of frequencies ranging from 750 kHz to 24 MHz and has a duration ranging from 1 µs to 4000 µs. (These options are set by the EPC660's firmware.) Figure 1 shows optical waveforms transmitted by the custom camera at 12 MHz as measured by a Thorlabs DET10A photodetector with 1 ns rise time. The ideal waveform would be a burst of square pulses going from zero to maximum amplitude. As shown, the 12 MHz waveforms have some overshoot but are reasonable approximations of a square pulse. 12 MHz was used for all of the tests described below unless otherwise noted.

The EPC660 evaluation kit uses a Texas Instruments BeagleBone Black (BBB) single-board computer as the interface between the EPC660 chip and a host computer. We wrote a Matlab GUI to configure the EPC660 through the BBB and to collect and display camera data returned by the BBB [9]. The GUI records up to 1000 DCS images at a time and produces histograms of the distributions of amplitude and depth estimates for each image.

3. EXPERIMENTS IN CLEAR WATER

Experiments were first performed in clear water in order to baseline the performance of the camera.

3.1 Experimental setup

Figure 2 shows the experimental setup for imaging and ranging a submerged object in clear water. The camera looked into the tank through a 30"x18"x½" polycarbonate single-pane window. The EPC660 chip and SigBoard controlled a single-

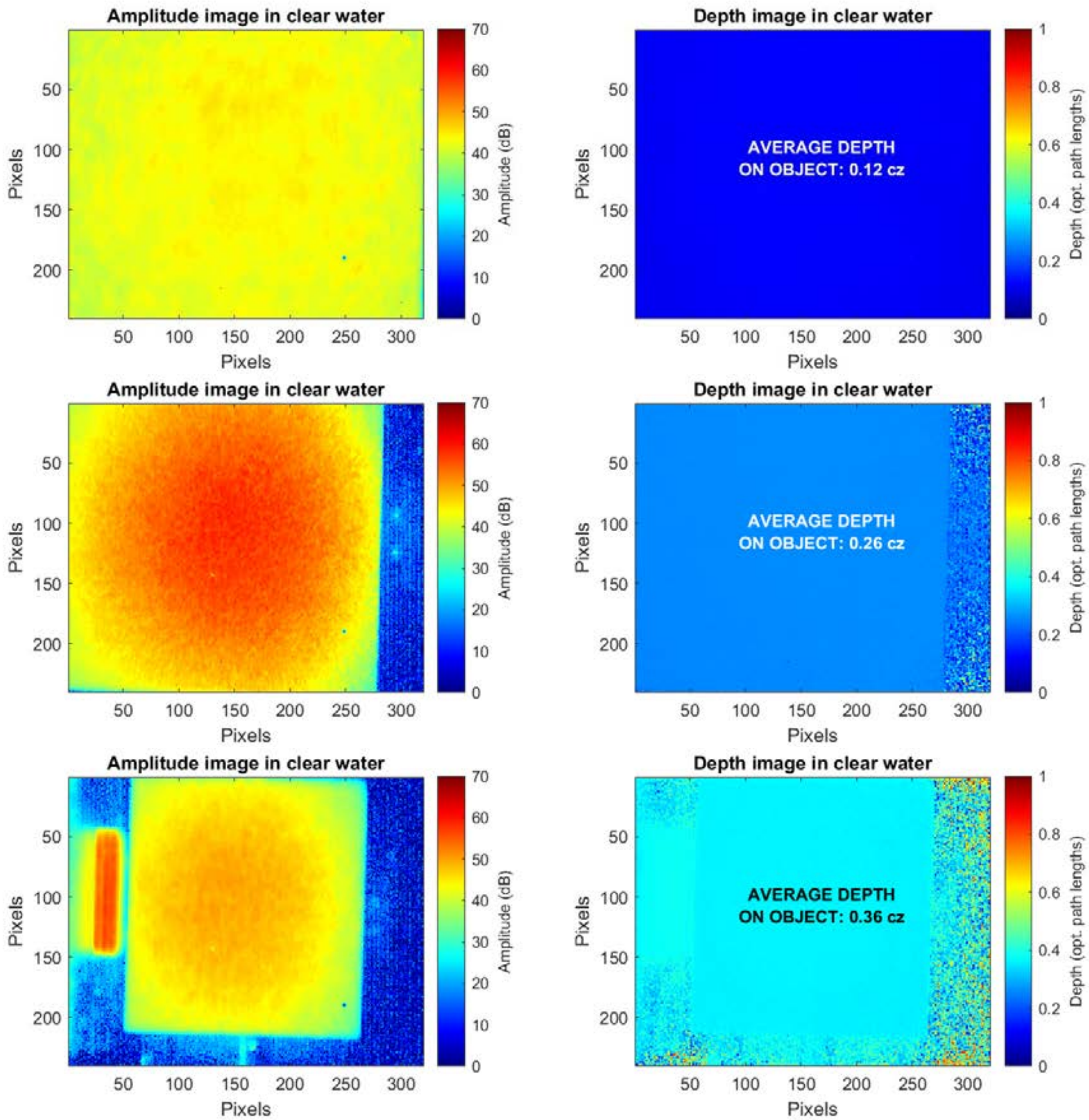

Figure 3. Amplitude and range images taken in clear water with 12 MHz modulation frequency and 4000 μs illumination time. *Left column:* Amplitude images showing the brightness of each pixel. In the middle image, the square gray plate is clearly brighter than the dark back of the tank. In the bottom image, a shiny metal piece to the left of the gray plate shows up brightly. *Right column:* Depth images showing the depth of each pixel. The depth of the object is uniform across the body of the gray plate, and is accurate to within 0.02 *cz*

laser LightBoard, which sent a collimated laser beam through an adjustable focusing lens into the water tank. A flat square plate of acrylic spray-painted matte gray was carried on a metal arm and hung from a motorized track into the tank. This plate was moved along the length of the tank by a motorized track. The lens was adjusted throughout the experiment to ensure most of the light hit the submerged plate. A Wetlabs AC-S transmissometer operating at 520 nm provided attenuation measurements (i.e. the exponential beam attenuation c coefficient with units of m^{-1}).

3.2 Sample images and range estimates

Figure 3 shows sample amplitude and depth images collected in clear water. These images were collected using a 12 MHz modulation frequency and a 4000 μs illumination time. The amplitude images have units of dB relative to one least significant bit (LSB) of the camera's digitizer. The amplitude images clearly show edges and features, and (unfortunately) show an exponential decay in brightness. Because of the exponential decay, we found that a logarithmic scaling worked well for the amplitude images. The depth images have units of optical attenuation lengths (cz, where c is the attenuation coefficient and z is the downrange distance), and showed good uniformity in depth estimate across the body of the plate. However, the depth of the low-amplitude pixels around the edge of the images was not valid, as the depth estimate was neither the distance to the back of the tank nor zero, either of which might have been considered valid.

To thoroughly test the accuracy of the camera's depth estimates in clear water, the gray plate was moved downrange and was imaged using 12 MHz frequency and 4000 μs duration. The average range of the central 50x50 pixels was considered the estimated depth of the object. Figure 4 shows the results. The measured distance generally tracked the actual object distance, but with a periodic error. This error was bounded by about ±3% of the distance measurement. This error is referred to in Espros's calibration application notes as the "DRNU error" and is present because our camera was not fully calibrated [10, 11]. The camera detected small movements of 0.001 *cz* change in depth.

3.3 Effect of illumination on range accuracy and image quality

The baseline ranging images were all taken with the object well-lit. In order to assess the effect of illumination on object amplitude and depth estimate accuracy, we next took images of the object at 0.5 *cz* downrange with progressively lower light levels. Illumination time was stepped down from 4000 μs to 10 μs, and the average amplitude and depth were calculated for the central 50x50 pixels in each image. Figure 5 shows the results. The image amplitude varied linearly as expected. The depth estimate should have been constant across all illumination time, but instead it dropped when the amplitude fell below 75 least significant bits (LSB). When the amplitude went below 20 LSB, the depth estimate became erratic, first increasing and then decreasing. This is generally consistent with Espros's documentation for the EPC660 chip [12] and indicates that depth estimates for any given pixel cannot not be considered high accuracy if that pixel's amplitude is <75 LSB.

Decreasing the illumination time also reduced image quality. Figure 6 shows that at low illumination levels object features drop below the noise floor, which has not only the typical salt-and-pepper image noise, but also FPN defined by vertical bands and a distinct quadrant pattern in the center of the image. These FPN features are consistent with other investigations [13] and were consistent throughout our work.

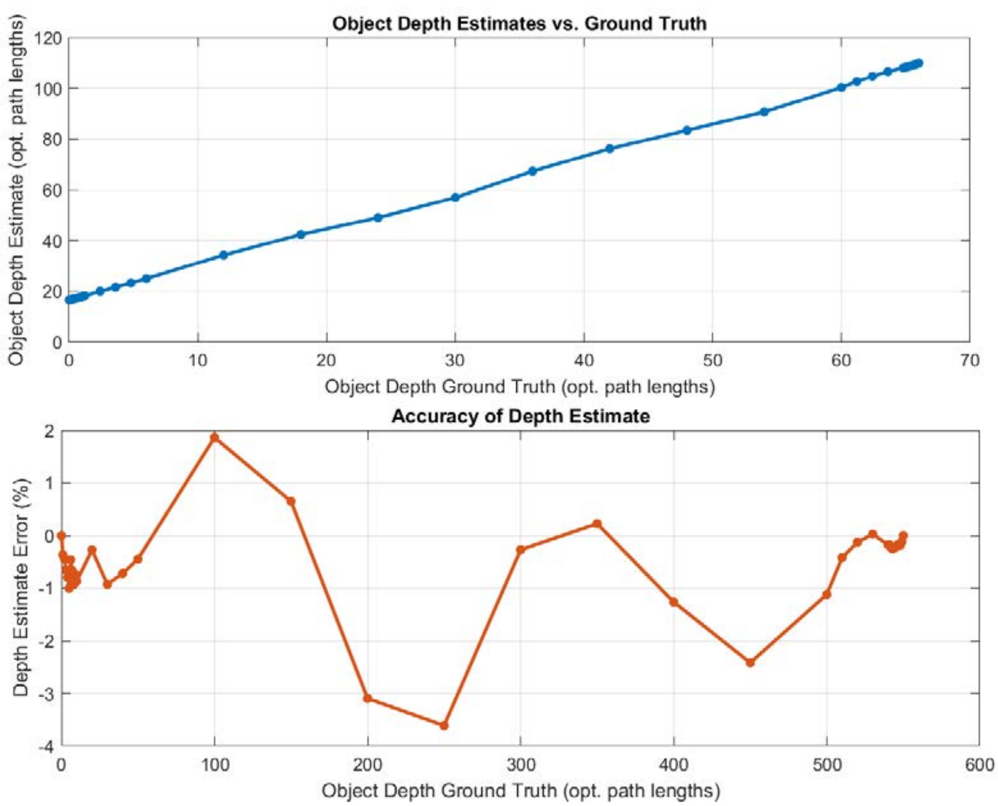

Figure 4. Ranging measurements in clear water using 12 MHz frequency and 4000 μs illumination time. *Top*: Depth estimates versus actual object depth, showing good object tracking and a resolution of small (~0.001 *cz*) object movements. *Bottom*: Depth estimate error. The trend is periodic, consistent with Espros's documented "DNRU error".

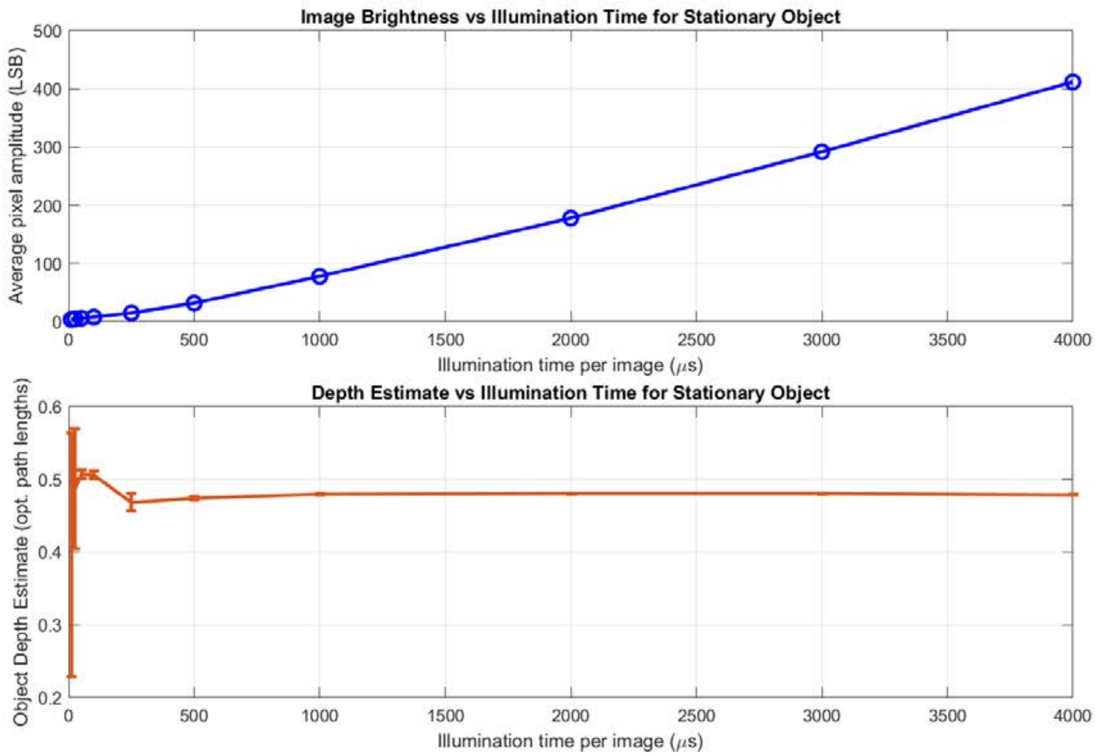

Figure 5. Effect of varying the illumination level (12 MHz, clear water, object at 0.48 *cz*). *Top:* The amplitude varies linearly with illumination. *Bottom:* The range is stable at high illumination but becomes erratic at low illumination. The error bars bound the 95% confidence interval of the estimates.

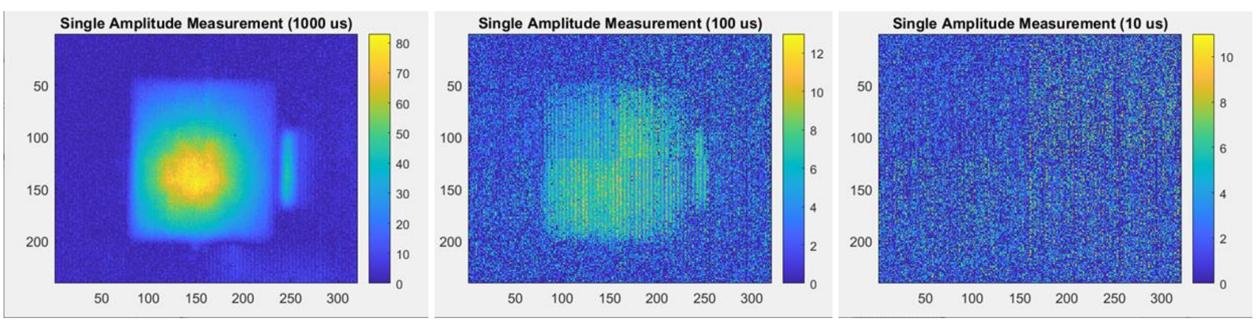

Figure 6. Effect of varying the illumination level (12 MHz, clear water, object at 0.48 *cz*) on image quality. *Left:* The object is seen clearly at 1000 µs illumination time. *Middle:* At 100 µs object features are lost and strong FPN appears. *Right:* At 10 µs the object disappears. Weak FPN and salt-and-pepper noise remain.

3.4 Averaging to improve illumination

We attempted to address low illumination levels by averaging the raw DCS images before constructing the range and amplitude images. We did this by collecting many images of the flat object fully filling the camera's view at varied illumination levels. However we found that averaging the DCS images did not represent coherent averaging. We compared averaged low-illumination images to single high-illumination images. Even when the averaged images together represented orders of magnitude more illumination time than did a single un-averaged image, the image quality of the averaged images was much worse (mostly because of the presence of the stable FPN) and the signal-to-noise ratio (SNR) of the depth estimate was lower.

3.5 Reduction of fixed pattern noise using digital filtering

The FPN that degraded image quality at low illumination levels was noted to have stable spatial frequency characteristics, and these were confined to relatively few frequencies. Thus we applied a frequency-domain finite impulse response (FIR) bandstop filter to the camera images to remove the FPN frequencies [14, 15]. This resulted in improved images with less FPN without reducing feature quality. Figure 7 shows a raw image set taken with low illumination before and after the FIR filter was applied.

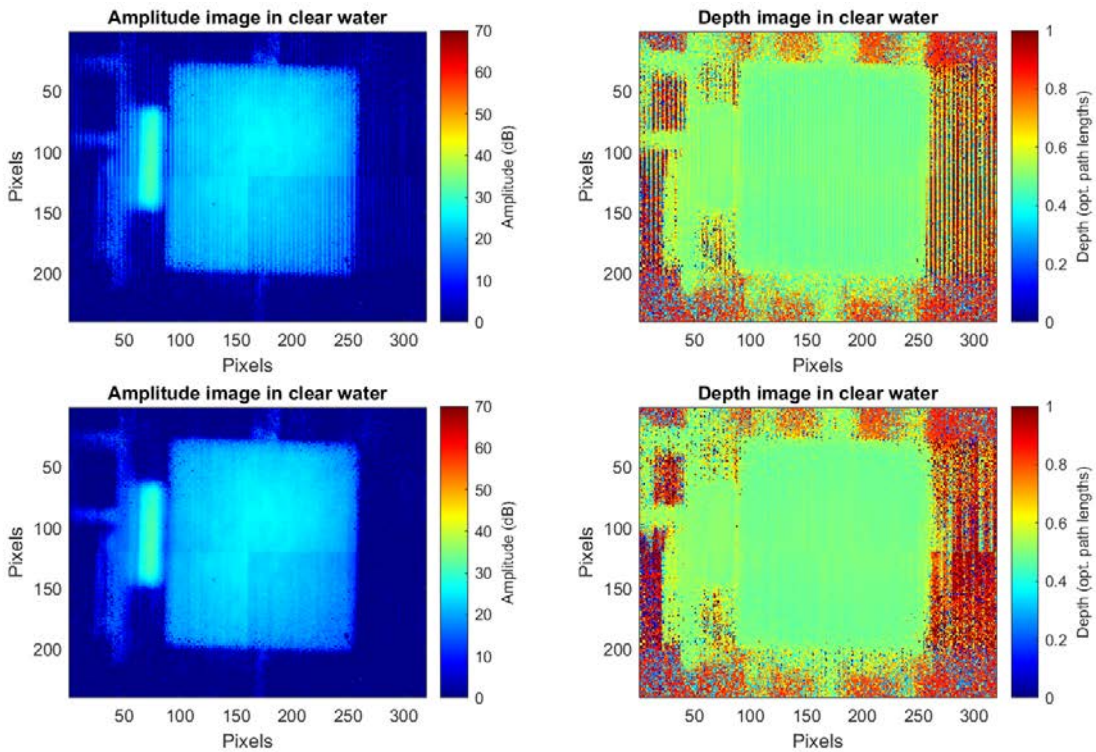

Figure 7. Reduction of FPN using FIR filter. *Top row:* Amplitude and range images taken at low illumination level, showing FPN vertical banding and a quadrant pattern. *Bottom row:* Amplitude and range image after a multi-band bandstop FIR filter was used to remove energy at the FPN's spatial frequencies. The quadrant effect remains.

4. EXPERIMENTS IN TURBID WATER

4.1 Experimental setup

Figure 8 shows the experimental setup for imaging and ranging a submerged object in turbid water. We started experiments with a one-laser LightBoard (see Figure 2) but after realizing the importance of illumination level we built a three-laser LightBoard and used it for most turbid water experiments. We placed diffusers over the lasers for some experiments, and removed them for other experiments. Turbidity was increased by adding Equate-brand liquid antacid to the tank. For most turbid water experiments, a Wetlabs C-star transmissometer operating at 470 nm provided attenuation measurements (the AC-S having been sent out for repair in between test sessions).

4.2 Depth images in turbid water

Depth images were taken in turbid water of the object at a fixed position. A single laser was used with an adjustable lens (as in Figure 2). Figure 9 shows depth error images collected in clear water and in increasingly turbid water. In these images, depth error was the difference between the known optical path lengths to the object and the depth estimated. Error statistics were calculated for the depth estimates of pixels on the body of the object.

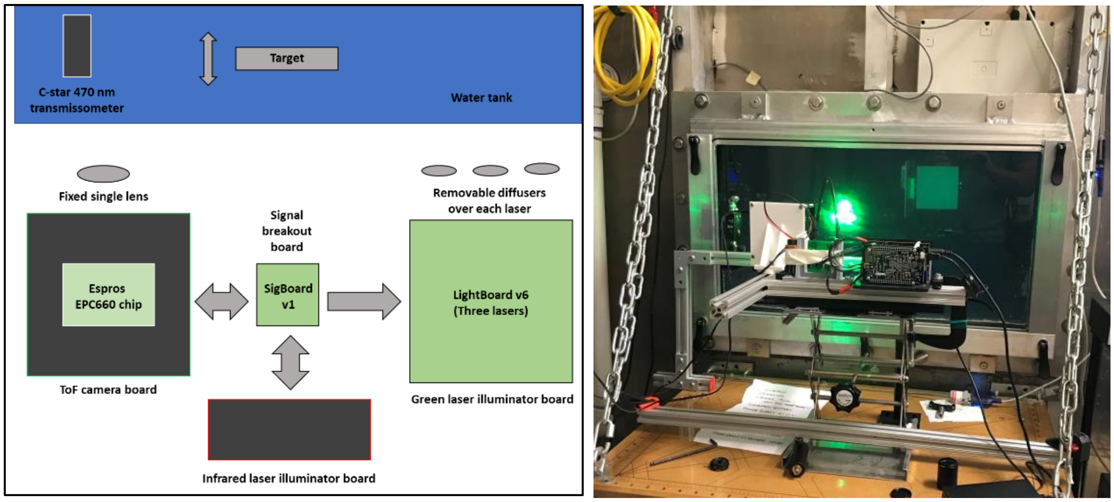

Figure 8. Experimental setup for clear water baseline experiments. *Left:* Block diagram for experiments. *Right:* Photograph of camera looking into input window of water tank.

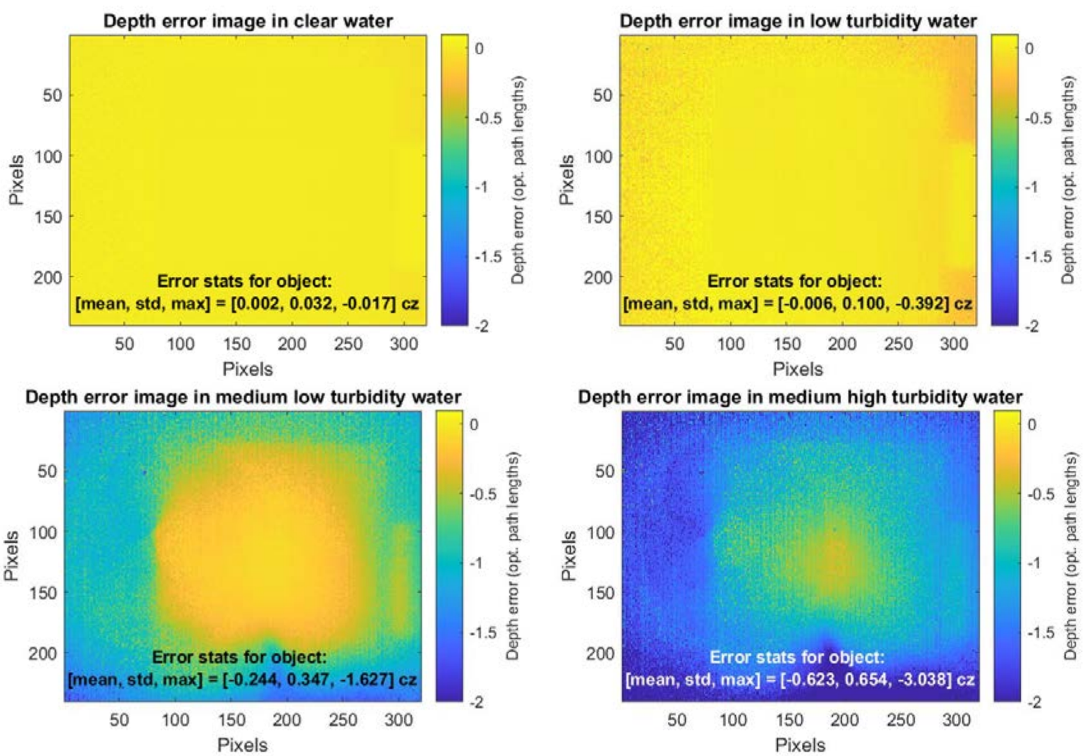

Figure 9. Effect of varying the turbidity level on depth images (12 MHz, 4000 µs, object at a fixed distance). *Top left:* Clear water. *Top right:* Low turbidity water. *Bottom left:* Medium low turbidity water. *Bottom right:* Medium high turbidity water. Increasing turbidity increases the backscatter contribution to each pixel. This results in depth estimates skewed negatively (i.e, towards the camera). The effect is least pronounced near the center of the object because the beam is brightest there.

The primary effects on the depth estimates of increasing turbidity were: 1) an increase in the standard deviation of the depth estimates and 2) a negative skew of the depth estimates of individual pixels. This latter effect happened at low turbidities for the low-amplitude pixels around the edge of the image and at higher turbidities for the high-amplitude pixels in the middle of the object image. We attribute this negative skew to the collection of photons backscattered from suspended particles, as these photons would have had shorter time-of-flight than photons reflected from the object. The backscatter photons skewed the phase measurement and thus the depth estimate negatively towards the camera. The medium high turbidity image of Figure 9 highlights the phenomenon: around the edge of the image, the only major contributor to the phase measurements is backscatter, and so the depth estimate is low. On the gray object, both strong reflection and backscatter contribute to the phase measurements, and so the depth estimates are high, though still lower than those in the clear water image. The depth error is smallest where the object reflection is brightest.

4.3 Ranging using collimated laser beams

The effects of backscatter on the depth estimates shown in Figure 9 were broadly distributed across each image. This is presumably because the object was illuminated with a broad cone of light generated using a single laser beam and an adjustable diverging lens. We performed a second ranging experiment in turbid water using the three-laser LightBoard, with collimated laser beams (i.e. no diffuser or lens). This arrangement resulted in a much different relationship between backscatter and object reflection, as shown in Figure 10. The beams came into the camera's field of view from the left side, and a strong but highly localized backscatter was observed there. The beams hit the object in three places and created spots of high illumination. The result of this localized backscatter and localized object illumination was that the images of the object beam spots were not affected much by the backscatter and so their depth estimates had high accuracy. The images of the rest of the object had mixed low contribution from the backscatter and the object so they had low depth estimate accuracy.

This approach trades away the possibility of clearly imaging object features in exchange for accurate ranging at longer optical path lengths in turbid water. By localizing the backscatter and the object, the accuracy of the beam spots is retained. Figure 11 and Figure 12 show data from this same experiment and reinforce the observations. When the object is at 3.6 *cz*, most of the object body has high depth estimate error, but the marked beam spot on the object is accurate to 1%. When the object is at 4.6 *cz*, the marked beam spot's depth estimate is still accurate to within 2% error despite being very dim.

This experiment also indicated that if the camera were to be used for long-range detection in turbid water, it would be preferable to use collimated laser beams and perform detection on the range images, as these images seemed to have a higher sensitivity than the amplitude images.

4.4 Effect of changing modulation frequency on the depth estimates

In the final experiment conducted in turbid water, the modulation frequency of the illuminator was changed and the effect on the object and backscatter portions of the depth images was observed. This experiment was conducted with three collimated laser beams, the object at 4.55 *cz*, and medium-low turbidity water. Figure 13 shows the cases where the modulation frequency was set to 3 MHz and 12 MHz. In both cases, the measured range to the beam spots on the object are similar: 4.83 *cz* and 4.76 *cz*. However, the measured range to the beginning of the backscatter beam in the two images is much different: 2.11 *cz* versus 1.76 *cz*. Thus while the object depth estimate changed by 1.5%, the backscatter depth estimate changed by 20%. Similar differences were seen along the length of the beam. We hypothesize that this effect is due either to increasing backscatter decorrelation at higher frequencies [16], or due to reduced amplitude at increasing modulation frequencies. (As in Figure 5, the depth estimates can change suddenly as amplitude drops below 75 LSB, and this effect may be contributing here.) Pending further understanding of physical origin, this phenomenon may be useful in isolating object depth estimates. Collecting images at multiple frequencies might allow pixels with stable depth estimates to be considered object pixels, while those with unstable depth estimates could be considered backscatter or noise pixels and discarded.

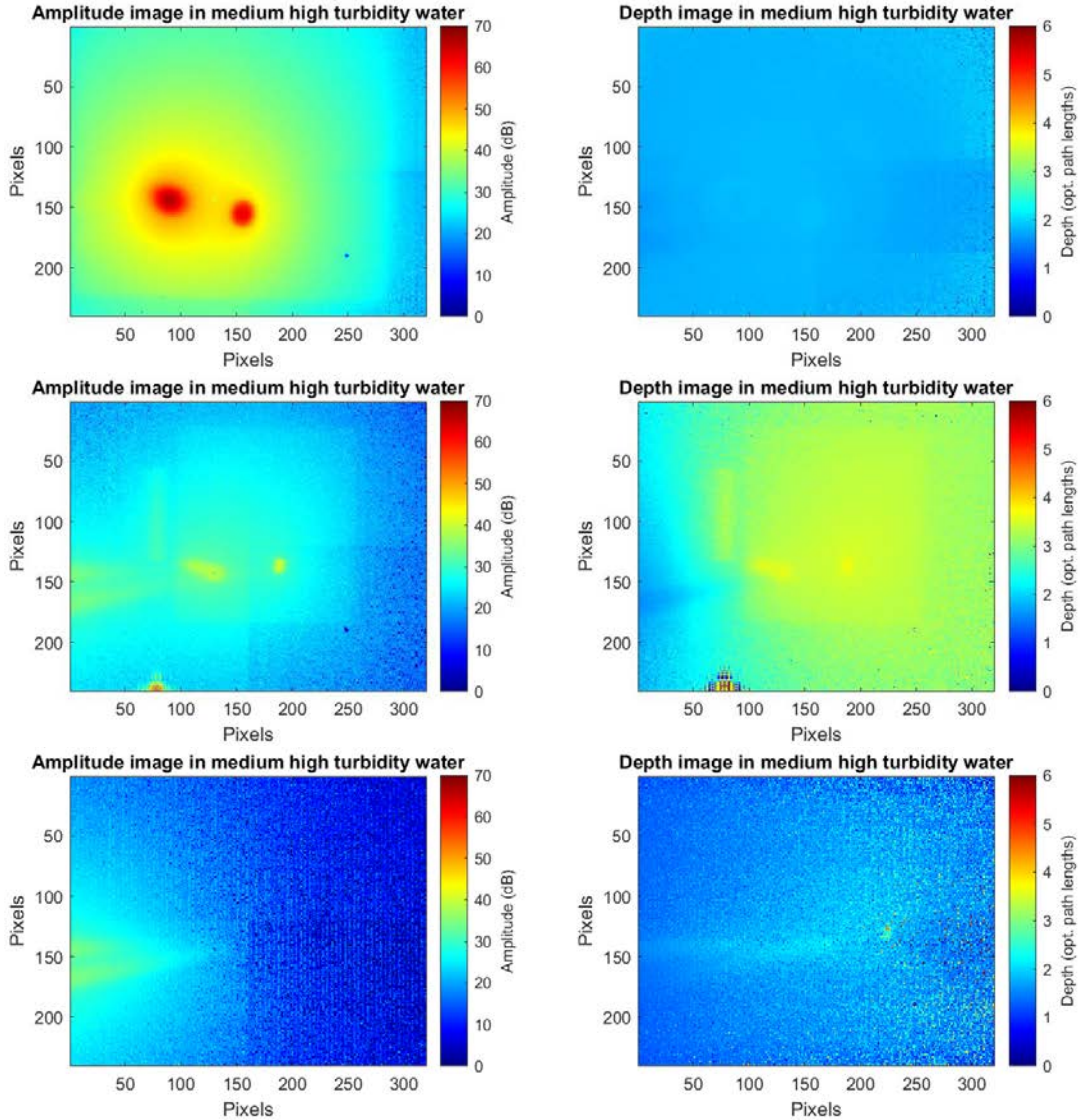

Figure 10. Images taken with three collimated lasers in medium-high turbidity water. *Left column*: Amplitude images for object distances of 1.8 *cz*, 3.6 *cz*, and 5.4 *cz*. The laser beam shows up on the left side of the image in the middle and bottom images. Beam spots on the object show up in the top and middle images. *Right column:* Depth images for object distances of 1.8 *cz*, 3.6 *cz*, and 5.4 *cz*. The middle image shows the backscatter from the beam and the object reflection at the beam spots, and a region where the contributions are mixed. The bottom image shows object beam spots strong enough to support detection, although no such spot appears in the corresponding amplitude image.

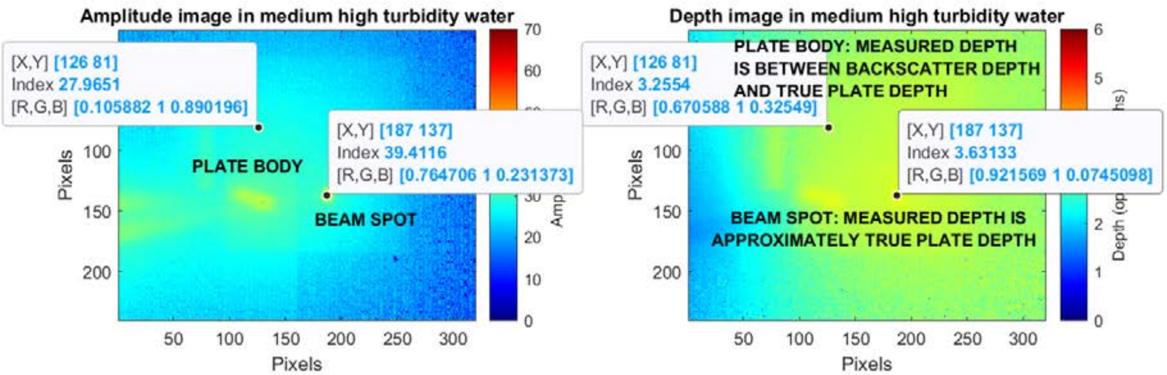

Figure 11. Showing beam spot accuracy for object distance of 3.64 *cz* with three collimated lasers in medium-high turbidity water (12 MHz, 4000 µs). *Left:* Amplitude image showing backscatter from laser, weakly illuminated object, and three beam spots on object. *Right:* Depth image showing that the object body has inaccurate depth estimates due to backscatter contribution, but the beam spots have accurate depth estimates (<1% error) as the object reflection there is much stronger than the backscatter.

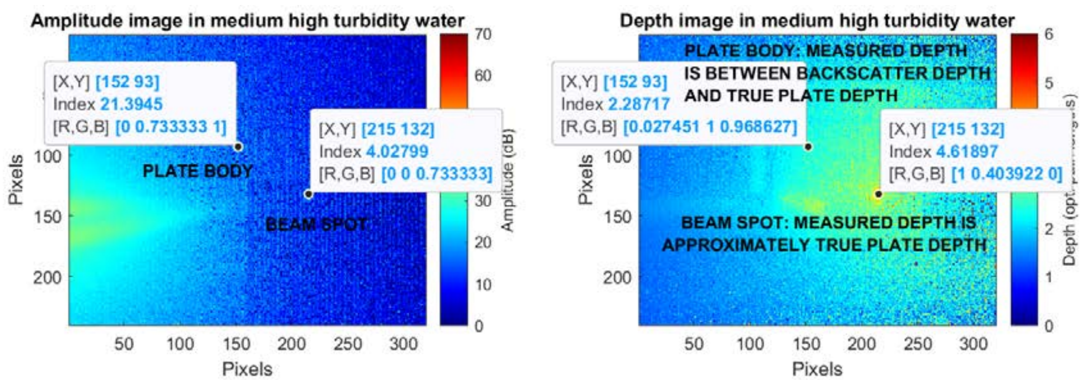

Figure 12. Showing beam spot accuracy for object distance of 4.55 *cz* with three collimated lasers in medium-high turbidity water (12 MHz, 4000 µs). *Left:* Amplitude image showing backscatter from laser, weakly illuminated object, and three beam spots on object. *Right:* Depth image showing that while the object body has inaccurate depth estimates, the beam spot error is <2%.

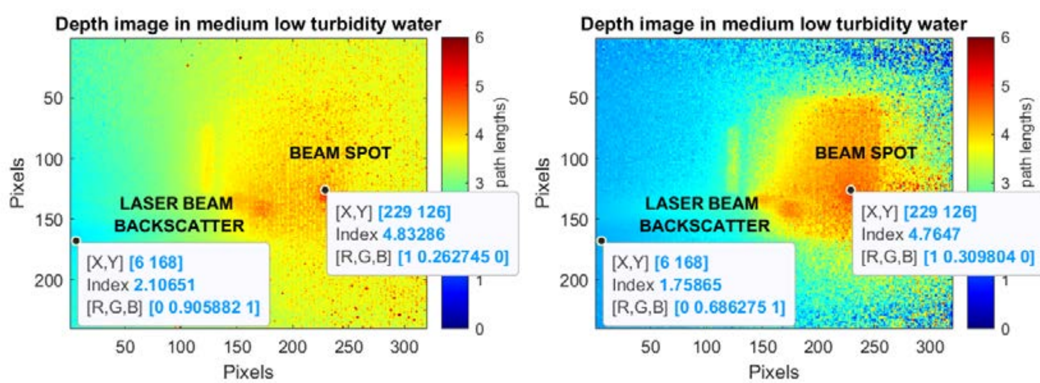

Figure 13. Change in backscatter depth estimate with modulation frequency (medium-low turbidity water, 4000 µs, object at 4.55 *cz*). *Left:* Depth image taken using 3 MHz frequency. *Right:* Depth image taken using12 MHz frequency. The depth estimate of the object beam spot changes by 1.5% while the backscatter depth estimate changes by 20%.

5. CONCLUSIONS

Our experiments showed that the EPC660 ToF sensor can be used underwater by using visible light lasers and modified receiver optics. The modified camera worked well in clear water for amplitude and depth imaging and ranging, provided that the illumination level was sufficiently high. At low illumination levels we observed difficulties with FPN and incorrect depth estimates. We were not able to eliminate FPN by averaging raw camera images, but we were able to reduce its effect by applying frequency-domain image filtering. In turbid water, we initially transmitted a cone of light to provide uniformly high illumination levels. This approach allowed imaging but resulted in backscatter contribution across the entire field of view and thus we observed large depth estimate errors. When we transmitted collimated beams of light, we were not able to image the object but depth accuracy was satisfactory at the spots where the beams illuminated the object. With collimated beams, we were able to estimate the depth of a gray object at 4.5 optical attenuation lengths away from the camera in moderately turbid water with about 1% range error.

Our experiments suggest that ToF cameras may be readily used in clear water for imaging, ranging, and mapping so long as sufficient illumination levels are maintained. They seem also to be directly usable in turbid water for short optical distances, where the object reflection can be much brighter than the backscatter. At longer optical path lengths and/or high turbidities, we would propose using ToF cameras with collimated laser beams as convenient and sensitive ranging sensors. However, we would be cautious using them for imaging without additional measures to reduce the backscatter contribution to the depth estimates. Backscatter mitigation may come in part from the use of multiple frequencies to form images.

ACKNOWLEDGEMENTS

Funding for this project was provided in part by ONR grant N00014-18-1-2291. Any opinions, findings, and conclusions or recommendations expressed in this material are those of the authors and do not necessarily reflect the views of the Office of Naval Research.

REFERENCES

[1] May, S., Dröschel, D., Fuchs, S., Holz, D. and Nüchter, A., 2009, October. Robust 3D-mapping with time-of-flight cameras. In *2009 IEEE/RSJ International Conference on Intelligent Robots and Systems* (pp. 1673-1678). IEEE.

[2] For example, the PMD Technologies product line. https://pmdtec.com/en/ (Accessed: 17-Feb-2022).

[3] Larry Li (Texas Instruments, Inc). “Time-of-flight camera – An introduction”. https://www.ti.com/lit/wp/sloa190b/sloa190b.pdf (Accessed: 17-Feb-2022).

[4] Melexis, Inc. “Application note: Time of Flight Basics”. https://www.melexis.com/en/documents/documentation/application-notes/application-note-time-of-flight-basics (Accessed: 17-Feb-2022).

[5] For example, the MLX75027 VGA time-of-flight sensor has VGA resolution (640x480 pixels). https://www.mouser.com/datasheet/2/734/MLX75027_Datasheet_Melexis-1620814.pdf (Accessed: 17-Feb-2022).

[6] Naik, N., Kadambi, A., Rhemann, C., Izadi, S., Raskar, R. and Bing Kang, S., 2015. A light transport model for mitigating multipath interference in time-of-flight sensors. In *Proceedings of the IEEE Conference on Computer Vision and Pattern Recognition* (pp. 73-81).

[7] Mack, K.V., Athavale, P., Jemison, W.D., Illig, D.W., Rumbaugh, L.K., Banavar, M.K. and Bollt, E.M., 2021, April. Restoration of time-of-flight (ToF) underwater images using TV regularization. In *Ocean Sensing and Monitoring XIII* (Vol. 11752, p. 117520N). International Society for Optics and Photonics.

[8] Espros, Inc. https://www.espros.com/photonics/epc660-evaluation-kit/ (Accessed: 17-Feb-2022).

[9] Joshua Thomson, Kevin Mack and Luke Rumbaugh (2022). TOF Capture Software (https://www.mathworks.com/matlabcentral/fileexchange/<...>), MATLAB Central File Exchange. Retrieved February 17, 2022.

[10] Dieter Kaegi (Espros, Inc). “Calibrating time-of-flight cameras”. https://www.autovision-news.com/wp-content/uploads/2020/02/ESPROS_Calibrating_TOF_cameras-2.pdf (Accessed 17-Feb-2022).

[11] Espros, Inc. “Calibration and compensation of cameras using ESPROS TOF Chips”, https://www.espros.com/downloads/09_Application_notes/AN10_Calibration_and_Compensation_Notice.pdf. Obtainable by contacting sales@espros.com. (Accessed 17-Feb-2022).

[12] Espros, Inc. “Datasheet – EPC 660 3D TOF imager 320x240 pixel”. https://www.espros.com/downloads/01_Chips/Datasheet_epc660.pdf (Accessed 17-Feb-2022).
[13] Georgiev, M., Bregović, R. and Gotchev, A., 2015. Fixed-pattern noise modeling and removal in time-of-flight sensing. *IEEE Transactions on Instrumentation and Measurement*, *65*(4), pp.808-820.
[14] Saramaeki, T., Mitra, S.K. and Kaiser, J.F., 1993. Finite impulse response filter design. *Handbook for digital signal processing*, *4*, pp.155-277.
[15] Mathworks, documentation for the `fwind2` Matlab function. https://www.mathworks.com/help/images/ref/fwind2.html (Accessed 17-Feb-2022).
[16] Pellen, F., Intes, X., Olivard, P., Guern, Y., Cariou, J. and Lotrian, J., 2000. Determination of sea-water cut-off frequency by backscattering transfer function measurement. *Journal of Physics D: Applied Physics*, *33*(4), p.349.